

The role of lattice mismatch on the emergence of surface states in 2D hybrid perovskite quantum wells

M. Kepenekian,^{1,*} B. Traore,¹ J.-C. Blancon,² L. Pedesseau,³ H. Tsai,^{2,4} W. Nie,² C. C. Stoumpos,⁵
M. G. Kanatzidis,⁵ J. Even,³ A. D. Mohite,² S. Tretiak,^{2,†} and C. Katan^{1,‡}

¹Univ Rennes, ENSCR, INSA Rennes, CNRS, ISCR – UMR 6226, F-35000 Rennes, France

²Los Alamos National Laboratory, Los Alamos, NM 87545, USA

³Univ Rennes, INSA Rennes, CNRS, FOTON – UMR 6082, F-35000 Rennes, France

⁴Department of Materials Science and Nanoengineering, Rice University, Houston, TX 77005, USA

⁵Department of Chemistry, Northwestern University, Evanston, IL 60208, USA

Surface states are ubiquitous to semiconductors and significantly impact the physical properties and consequently the performance of optoelectronic devices. Moreover, surface effects are strongly amplified in lower dimensional systems such as quantum wells and nanostructures. Layered halide perovskites (LHPs) are 2D solution-processed natural quantum wells,^{1–3} where optoelectronic properties can be tuned by varying the perovskite layer thickness. They are efficient semiconductors with technologically relevant stability.^{4–7} Here, a generic elastic model and electronic structure modelling are applied to LHPs heterostructures with various layer thickness. We show that the relaxation of the interface strain is triggered by perovskite layers above a critical thickness. This leads to the release of the mechanical energy arising from the lattice mismatch, which nucleates the surface reorganization and consequently the formation of lower energy edge states. These states, which are absent in 3D perovskites, dominate the optoelectronic properties of LHPs and are anticipated to play a crucial role in the design of LHPs for optoelectronics devices.

Surfaces and interfaces are known to play a central part in the performances of classical semiconductor based devices.^{8–10} This holds true for the recently emerged halide perovskites.^{11,12} The 2D members of the family, layered halide perovskites (LHPs) have superior photo- and chemo- stability compared to their 3D counterparts. They show strong promise in high performance optoelectronic devices such as photovoltaics, field effect transistors, electrically injected light emission and polarized optical spin injection.^{4–7,13,14} Their properties depend on the number n of MX_6 octahedra that span the perovskite layer (M is a metal, X a halogen). As in classical semiconductors,⁹ surface and interface structures can have a strong influence on the properties of LHPs.¹⁵ While experimental results exist, especially in Ruddlesden-Popper perovskites (RPPs) of general formula $\text{A}'_2\text{A}_{n-1}\text{M}_n\text{X}_{3n+1}$ (A and A' being cations), there is no simple model to predict and control LHP surface properties. Here, we show that optical properties of RPPs are decisively impacted by surface relaxations occurring for structures with $n > 2$. We rationalize these features by considering LHPs as heterostructures built from the $n=1$ monolayered perovskite $\text{A}'_2\text{MX}_4$ and the $n=\infty$ 3D AMX_3 . This picture leads to understanding of physical phenomena underpinning surface reconstruction and concomitant modifications of electronic structure, and allows to formulate the design principles of LHP materials optimized for optoelectronics, solid-state lighting or photovoltaics.

We start with evaluating the elastic energy density accumulated in LHPs by developing an elastic model for

the bulk structure (see [Method](#) and [Supplementary Information](#) for details). Our model was constructed based on the theory of elasticity in classical semiconductor heterostructures¹⁶ by identifying the LHP structure with a multi-quantum well system ([Fig. 1a](#)) with alternating stacking of 3D perovskite layers L1 (AMX_3 , of thickness $n-1$) and of 2D perovskite monolayers L2 (single octahedron, $n=1$). This combination forms an interface between two structurally-different layers, equivalent to a so-called L1/L2 heterostructures with a coherent interface (lattices are continuous across the interface in two directions).¹⁷ To illustrate this general concept, we consider the family of RPP of general formula $(BA)_2(MA)_{n-1}Pb_nI_{3n+1}$ that can be synthesized in phase-pure form (only one n -value).^{18–20}

[Fig. 1b](#) represents experimentally observed variations of the in-plane average lattice parameter as a function of n for the native $(BA)_2(MA)_{n-1}Pb_nI_{3n+1}$ heterostructure, as well as the out-of plane lattice parameters for the end members of the homologous series L1 ($(n-1)MAPbI_3$) and L2 ($(BA)_2PbI_4$). As qualitatively predicted based on elasticity, the in-plane lattice expansion from $n=1$ to $n=\infty$, gives rise to an out-of-plane lattice contraction in both L1 and L2 layers. However, the experimental variation of the in-plane parameter is noticeably steep, the in-plane parameter of $MAPbI_3$ ($n=\infty$) being almost already recovered for $n=2$. A similar steep variation is observed for the out-plane lattice parameter of the L2 layer. Interestingly, quantitative agreement between experimental results and elastic model predictions can only be obtained when a very low effective stiffness of the L2 layer is considered ([Fig. 1c](#)). The origin of such low stiffness can be traced back to the octahedra tilt angles extracted from the $(BA)_2(MA)_{n-1}Pb_nI_{3n+1}$ RPP experimental structures ([Table S1](#)). The octahedra tilt angles in L2 structure are indeed more important than in the L1 layers. In other words, the mechanical energy is more efficiently relaxed in the RPPs structures by rotation of those octahedra that are directly in contact with the flexible organic cations, than by Pb-I bond elongation.

Classic theory of elasticity predicts that, for a heterostructure L1/L2 with a large lattice mismatch between L1 and L2, the structure may undergo a reorganization for a critical layer thickness, to form nanostructures at the surface in order to relax the accumulated bulk mechanical energy.¹⁷ From the above results, the elastic energy density in RPPs with varying perovskite thickness n was computed ([Fig. 1d](#)). We observed a maximum elastic energy density of ~ 0.16 MPa for the RPP $n=2$, and a monotonic reduction of this energy with increasing n , which ultimately vanishes for bulk 3D perovskite ($n \rightarrow \infty$). Therefore, elastic energy density arising from the interface is expected to have direct consequences over surface properties for RPPs with low n -values.

We gained further microscopic insight by modelling the structural relaxation at the relevant surfaces of the $(BA)_2(MA)_{n-1}Pb_nI_{3n+1}$ RPP ($n=1-4$) using density functional theory (DFT), which allows direct simulation of all structural distortions (see [Method](#) for computational details). Applications using RPPs as active materials mainly employ two different orientations; either in-plane or out-of-plane with respect to the substrate or an interface layer ([Fig. 2a](#)). The most relevant surface of the RPP is then the (101) surface ([Fig. 2b](#)),^{4,15} which we model here on specifically designed slabs (see [Supplementary Text I](#) and [Fig. S4](#)), labelled as bulk-like and surface, for varying thickness $n=1$ to 4. The calculated changes in the surface structure were represented by (i) the contraction/expansion of the octahedron slabs close to the surface in the (101) direction ([Fig. 2c](#)), and (ii) the in-plane and out-of-plane tilting of the octahedra close to the surface ([Fig. 2d](#)).² This representation highlights our

early conclusion drawn from the elastic model that rotational degree of freedom of the octahedra play an essential role in relaxing the internal elastic energy, in contrast with classical semiconductor descriptions where local strain tensor suffices.²¹

Fig. 2c shows the variation along the (101) direction of the distance h between octahedral slabs close to the perovskite surface. The reference value of h is obtained from the bulk-like region fixed in our DFT calculations ($4 \leftrightarrow 5$ distance in Fig. 2c). The evolution of the inter-slab distance yields two opposite behaviours for $n=1,2$ and $n>2$. For $n>2$, the surface slab expansion is accompanied by a contraction of the sub-surface slabs, which leads to a decoupling of the top surface octahedron slab from the sub-surface ones. On the other hand, for $n=1,2$, expansion of octahedra slabs was observed in the entire surface region. A similar distinct behaviour between $n=1,2$ and $n>2$ was noted by analysing the surface relaxation in RPPs occurring through in-plane and out-of-plane tilting of octahedra (Fig. 2d). In fact, surface octahedra in $n=1,2$ yield almost no rotational degree of freedom, whereas $n>2$ systems exhibit significantly larger tilting of surface octahedra. The drastic change of surface behaviour, when increasing the perovskite layer thickness from $n=2$ to $n=3$ attests to a significant change of surface flexibility, which helps structural relaxation of the internal elastic energy.

We evaluate the impact of these surface relaxation processes on the electronic and optical properties of RPPs by comparing band structures and wavefunctions at the surface and in the bulk (Fig. 3). The electronic band structure still presents a direct bandgap at the surface as compared to the bulk but with variation of the bandgap energy (Fig. 3a,b and Fig. S5). We observe that the bandgap blueshifts by 70 and 150 meV for $n=1$ and 2 respectively and redshifts by 120 and 70 meV for $n=3$ and 4, respectively. The accuracy of our approach is supported by (i) the excellent agreement between the calculated exciton properties in the bulk-like region with previously reported experimental results for the same materials (see Supplementary Text II),²² and (ii) the similar pattern in the optical bandgap shift between the RPP layer surface with respect to the bulk (Fig. S6).¹⁵ According to surface relaxation results, lattice expansion at the (101) surface with relatively small octahedral tilting leads to a bandgap blueshift, whereas sub-surface lattice compression with significant octahedral distortions results in a redshift of the bandgap due to appearance of in-gap electronic states.

In order to understand the microscopic impact of the structural changes at the surface on each type of charges, localized density of states (LDOS) of the valence band maximum (hole) and conduction band minimum (electron) were computed (Fig. 3c and Fig. S7a,b). For all n -values, surface relaxation leads to hole wavefunctions repelled away from the surface to the bulk. A similar behaviour is observed for electrons for $n=1,2$. In sharp contrast, for $n>2$, the electron gets localized mainly at the top (101) surface slab. Concomitantly, the preferential direction of electronic coupling switches from (010) to (101). From the barycenters of electron (z_e) and hole (z_h) LDOS profiles (Fig. S7c,d), we inspect separation of carriers ($\Delta z_{e/h} = z_e - z_h$) and demonstrate that upon appearance of in-gap states, the electron and hole get separated (Fig. 3d). The effect is maximum for $n=3$, $\Delta z_{e/h} = 13.2 \text{ \AA}$ (5.5 \AA for $n=4$). Its impact on optical activity is estimated by computing Kane energies²³ for bulk-like and relaxed slabs (see Method and Table S3). They reflect oscillator strengths of the optical-transitions and show a systematic reduction by 50%, 85%, 30% and 95% for the 4 lowest excitations of $n=3$ RPP (Table S3). Such electron-hole

separation at the surface is consistent with the longer photoluminescence lifetime of low-energy states reported recently.¹⁵ Fig. 3e summarizes our understanding of the formation of these low-energy states (LES) in RPPs with $n > 2$, which primarily stems from surface relaxation that strongly localizes the electron at the surface and facilitates dissociation of the strongly bound bulk exciton.

LES result from the release of the strain-induced elastic energy at the L1/L2 interface (Fig. 1). From our elastic model, the amount of energy accumulated in the materials is directly dependent on the amplitude of lattice mismatch between layers in the heterostructure L1/L2 and as a result, tuning the RPP structure and composition can lead to drastic changes of surface properties. Using this general approach, the internal elastic energy density accumulated in the bulk of LHPs can be estimated for any composition and perovskite layer thickness. From a practical perspective, understanding the relaxation of the stored elastic energy at the surface of the LHP materials is of paramount importance and presents a perfect platform for the systematic and comprehensive evaluation and screening of LHP compounds with defined functionalities for novel devices. This concept is illustrated by changing organic cation A' in RPPs (Fig. 4a). For example, replacing BA with $C_9H_{19}NH_3$ (NoA), which has a significantly smaller lattice mismatch,²⁴ results in the reduction of the elastic energy density of the RPP composite by more than an order of magnitude (Fig. 4b). This would prevent formation of LES and preserve the bulk Wannier exciton. By contrast, RPPs based on an organic cation inducing a larger mismatch, namely $(4Cl-C_6H_4NH_3)_2PbI_4$ (4Cl-PhA),²⁵ undergoes increased strain (Fig. 4a), thus larger elastic energy density that should favour significant (101) surface relaxation suitable for e-h carrier separation.

In summary, we simulated edge (surface) relaxation effects in layered hybrid perovskite materials and discovered a critical layer thickness above which the surface reorganization becomes significant. This consequently leads to the formation of lower energy electronic states rationalizing and confirming experimental observations.¹⁵ Our modelling is based on the first generic elastic model for LHPs accounting for the internal elastic energy accumulated in the material bulk and is further demonstrated using electronic structure calculations of the surface relaxation of perovskite layers. Our observation of electronic bandgap shifts and exciton dissociation at the surface, depending on the layered perovskite structure distinguishes these materials from their 3D $APbI_3$ (A=cation; $n=\infty$) counterparts and pave the way to unique tailored properties and functionalities for optoelectronic applications.

References

- [1] Saparov, B. & Mitzi, D. B. Organic-inorganic perovskites: Structural versatility for functional materials design. *Chem. Rev.* **116**, 4558–4596 (2016).
- [2] Pedesseau, L. *et al.* Advances and promises of layered halide hybrid perovskite semiconductors. *ACS Nano* **10**, 9776–9786 (2016).
- [3] Li, W. *et al.* Chemically diverse and multifunctional hybrid organic-inorganic perovskites. *Nat. Rev. Mater.* **2**, 16099 (2017).
- [4] Tsai, H. *et al.* High-efficiency two-dimensional ruddlesden-popper perovskite solar cells. *Nature* **536**, 312–317 (2016).
- [5] Yuan, M. *et al.* Perovskite energy funnels for efficient light-emitting diodes. *Nature Nanotech.* **11**, 872–877 (2016).
- [6] Wang, N. *et al.* Perovskite light-emitting diodes based on solution-processed self-organized multiple quantum wells. *Nature Photon.* **10**, 699–704 (2016).
- [7] Odenthal, P. *et al.* Spin-polarized exciton quantum beating in hybrid organic-inorganic perovskites. *Nature Phys.* **13**, 894–899 (2017).
- [8] Zwanenburg, F. A. *et al.* Silicon quantum electronics. *Rev. Mod. Phys.* **85**, 961 (2013).
- [9] del Alamo, J. A. Nanometre-scale electronics with III-V compound semiconductors. *Nature* **479**, 317–323 (2011).
- [10] Hwang, H. Y. *et al.* Emergent phenomena at oxide interfaces. *Nature Mater.* **11**, 103–113 (2012).
- [11] Haruyama, J., Sodeyama, K., Han, L. & Tateyama, Y. Surface properties of CH₃NH₃PbI₃ for perovskite solar cells. *Acc. Chem. Res.* **49**, 554–561 (2016).
- [12] Murali, B. *et al.* The surface of hybrid perovskite crystals: A boon or bane. *ACS Energy Lett.* **2**, 846–856 (2017).
- [13] Mitzi, D. B., Feild, C. A., Harrison, W. T. A. & Guloy, A. M. Conducting tin halides with a layered organic-based perovskite structure. *Nature* **369**, 467 (1994).
- [14] Kagan, C. R., Mitzi, D. B. & Dimitrakopoulos, C. D. Organic-inorganic hybrid materials as semiconducting channels in thin-film field-effect transistors. *Science* **286**, 945 (1999).
- [15] Blancon, J.-C. *et al.* Extremely efficient internal exciton dissociation through edge states in layered 2d perovskites. *Science* **355**, 1288–1292 (2017).
- [16] Vurgaftman, I. & Meyer, J. R. Band parameters for III–V compound semiconductors and their alloys. *J. Appl. Phys.* **89**, 5815 (2001).
- [17] Bimberg, D., Grundmann, M. & Ledentsov, N. N. *Quantum Dot Heterostructures* (John-Wiley and Sons, 1999).
- [18] Ruddlesden, S. N. & Popper, P. New compounds of the K₂NiF₄ type. *Acta Cryst.* **10**, 538–539 (1957).
- [19] Ruddlesden, S. N. & Popper, P. The compound Sr₃Ti₂O₇ and its structure. *Acta Cryst.* **11**, 54–55 (1958).
- [20] Stoumpos, C. C. *et al.* Ruddlesden-popper hybrid lead iodide perovskite 2d homologous semiconductors. *Chem. Mater.* **28**, 2852–2867 (2016).
- [21] Davies, J. H., Bruls, D. M., Vugs, J. W. A. M. & Koenraad, P. M. Relaxation of a strained quantum well at a cleaved surface. *J. Appl. Phys.* **91**, 4171–4176 (2002).
- [22] Blancon, J.-C. *et al.* Strongly bound excitons in ruddlesden-popper 2d perovskites, arXiv:1710.07653.
- [23] Kane, E. O. *Semiconductors and Semimetals* (Academic Press, 1966).
- [24] Lemmerer, A. & Billing, D. G. Synthesis, characterization and phase transitions of the inorganic-organic layered perovskite-type hybrids [(C_nH_{2n+1}NH₃)₂PbI₄], n=7, 8, 9 and 10. *Dalton Trans.* **41**, 1146–1157 (2012).
- [25] Liu, Z. *et al.* Crystal structure of bis(4-chloroanilinium) tetraiodoplumbate(ii), (ClC₆H₄NH₃)₂PbI₄. *Z. Kristallogr. NCS* **219**, 457–458 (2004).

Acknowledgements

The work in France was supported by Agence Nationale pour la Recherche (TRANSHYPERO project) and was granted access to the HPC resources of [TGCC/CINES/IDRIS] under the allocation 2017-A0010907682 made by GENCI. The work at Los Alamos National Laboratory (LANL) was supported by LANL LDRD program (J.-C.B., W.N., S.T., A.D.M.) and was partially performed at the Center for Nonlinear Studies. The work was conducted, in part, at the Center for Integrated Nanotechnologies (CINT), a U.S. Department of Energy, Office of Science user facility. Work at Northwestern University was supported by grant SC0012541 from the U.S. Department of Energy, Office of Science. C.C.S. and M.G.K. acknowledge the support under ONR Grant N00014-17-1-2231.

Author contributions

M. K., S.T. and C.K. conceived the idea, designed the work, and wrote the manuscript. J.E developed the semi-empirical BSE approach and the elastic model. M.K. performed the DFT calculations with support from B.T. and L.P. C.K. and M.K. analysed the data and provided insight into the mechanisms. M.G.K. and C.S.S. lend their expertise in chemistry. A.D.M., J.C., H. T. W. N. supplied knowledge from an application perspective. All authors contributed to this work, read the manuscript and agree to its contents, and all data are reported in the main text and supplemental materials.

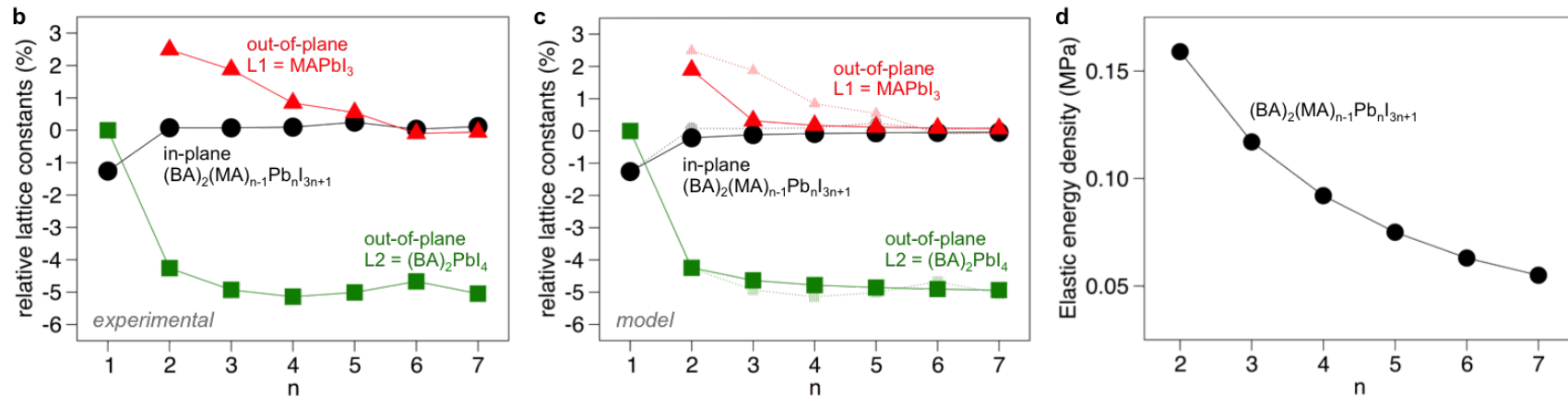
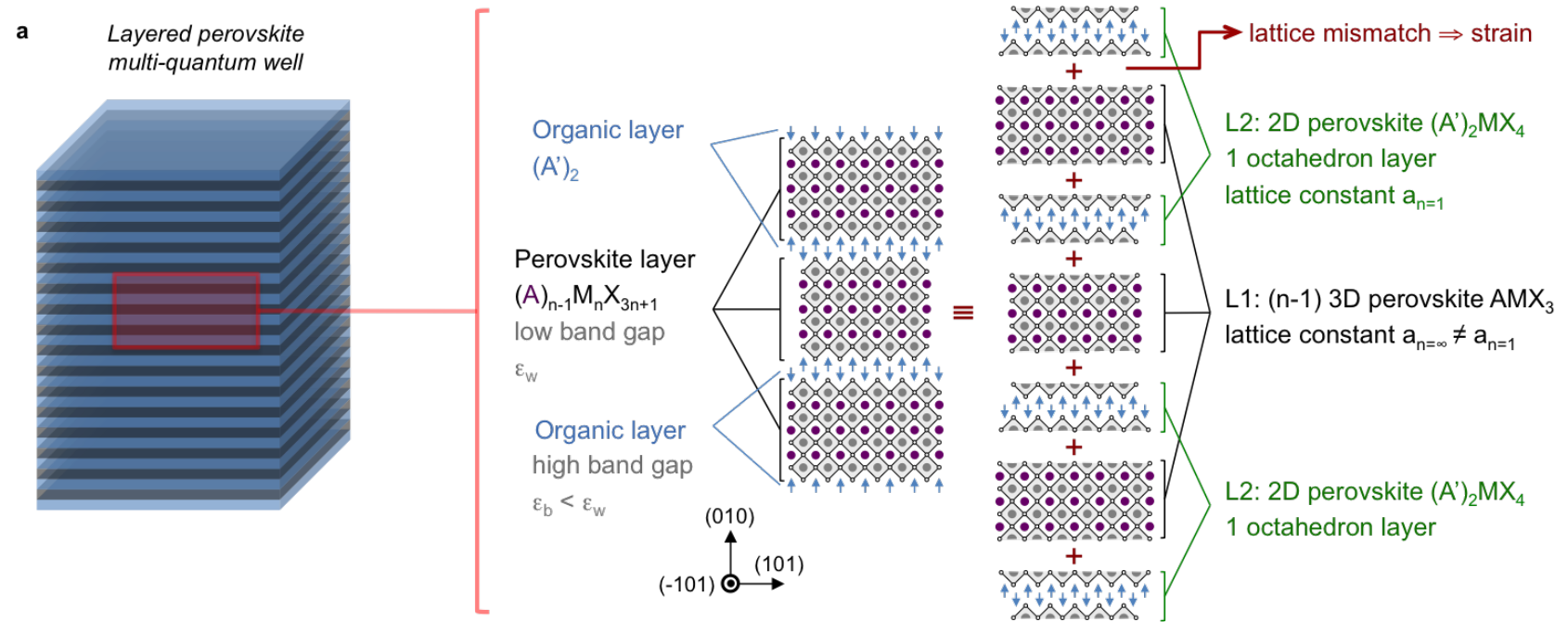


Figure 1 | LHPs generalized improper flexoelastic model. **a**, Schematics of hybrid layered compounds regarded as heterostructures L1/L2 with L1 the 3D ($n=\infty$) bulk materials, e.g. $MAPbI_3$, and L2, a $n=1$ compound, e.g. $(BA)_2PbI_4$. **b**, In-plane expansion and out-of-plane contractions of experimental lattice constants for $(BA)_2(MA)_{n-1}Pb_nI_{3n+1}$ and the L1 and L2 layers. The room-temperature structures of $MAPbI_3$ and $(BA)_2PbI_4$ serve as references for L1 and L2 structures, respectively. **c**, Same from the improper flexoelastic model (see [Method](#) for details). **d**, Computed elastic energy density for the $(BA)_2(MA)_{n-1}Pb_nI_{3n+1}$ heterostructure.

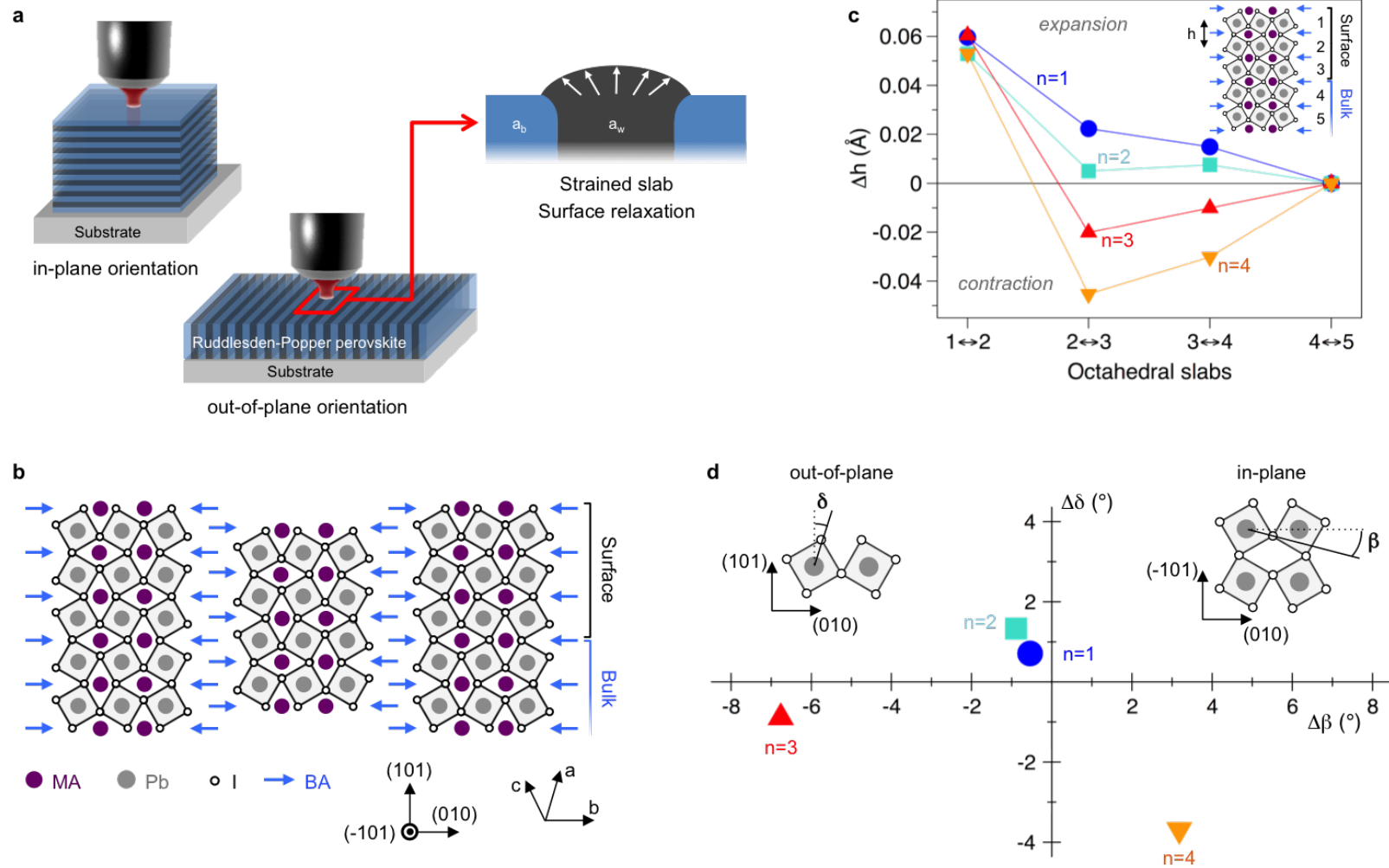


Figure 2 | Surface relaxation in LHP multi-quantum wells. **a**, Schematics of LHP-based devices in in-plane and out-of-plane orientation. **b**, Schematics of the (101) surface of the layered perovskite $(\text{BA})_2(\text{MA})_{n-1}\text{Pb}_n\text{I}_{3n+1}$ with $n=3$. **c**, Variation of the interlayer height difference (Δh) from bulk-like to surface (see inset). **d**, Variation of in-plane (β) and out-of-plane (δ) tiltings of surface octahedra due to the (101) surface relaxation.

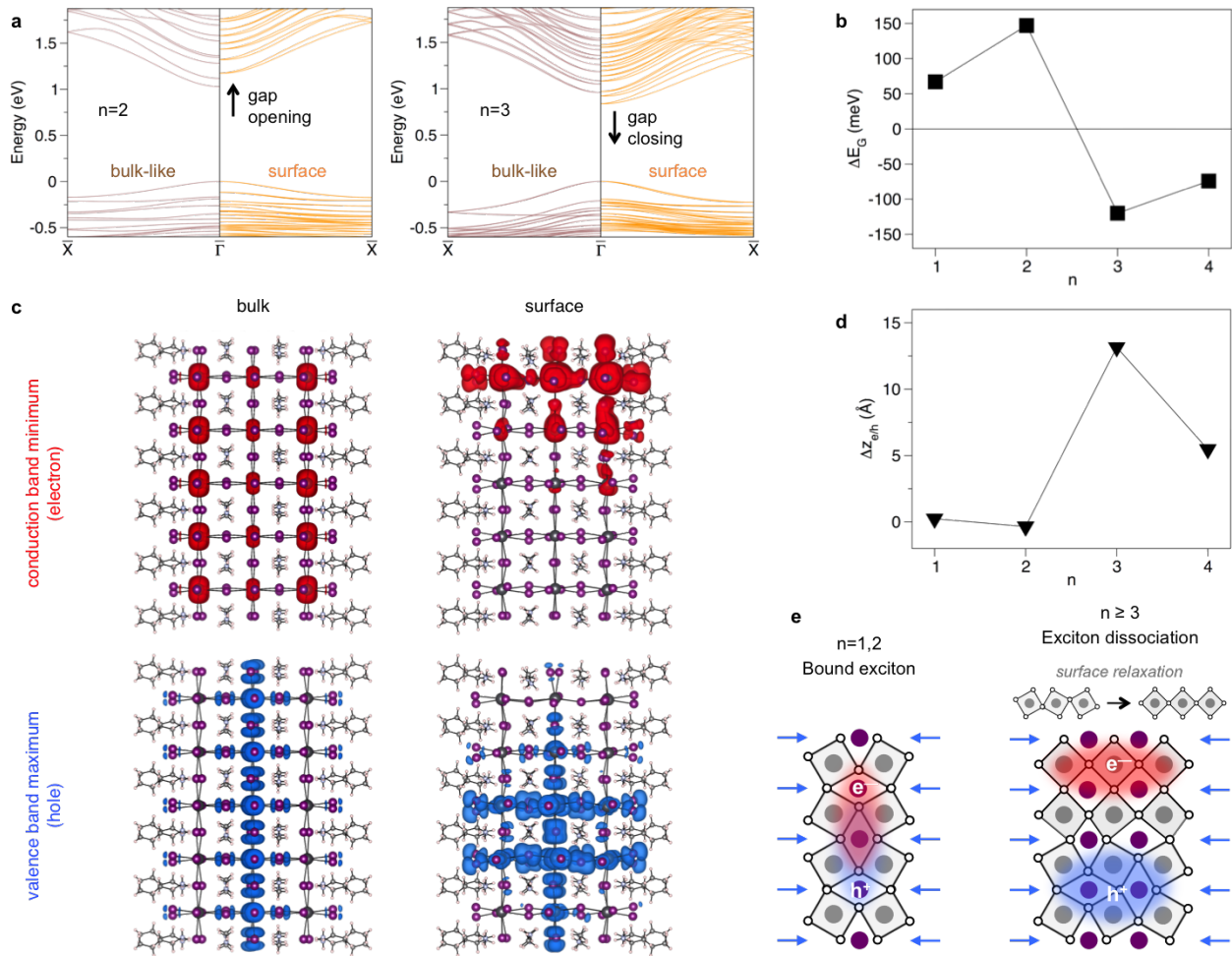


Figure 3 | Impact of surface structural relaxation on electronic and optical properties in $(\text{BA})_2(\text{MA})_{n-1}\text{Pb}_n\text{I}_{3n+1}$. **a**, Slab band structures in the bulk-like (left) and relaxed (101) surface (right) for $n=2$ and 3 . **b**, DFT variation of E_G going from bulk-like to relaxed (101) surface. **c**, Local densities of states (LDOS) computed at the valence band maximum and conduction band minimum for the $n=3$ RPP in bulk and relaxed surface. **d**, Difference between the barycenter of electron and hole wavefunctions. **e**, Schematics of the surface-induced exciton dissociation in RPPs with $n \geq 3$.

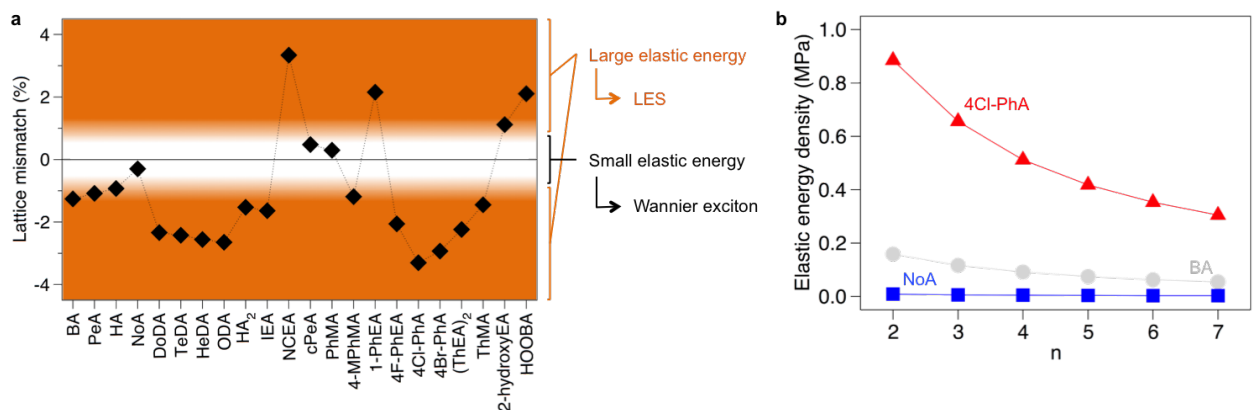


Figure 4 | Design of LHPs for photovoltaics and optoelectronics. **a**, Lattice mismatch between various monolayered $\text{A}'_2\text{PbI}_4$ perovskites ($n=1$) and MAPbI_3 (14cm ; $n=\infty$). All data are taken from X-ray structures resolved at room-temperature. Names for organic compounds and corresponding references are given [Table S4](#). **b**, Computed elastic energy density for heterostructures built with MAPbI_3 and $(\text{BA})_2\text{PbI}_4$ (grey line), $(\text{C}_9\text{H}_{19}\text{NH}_3)_2\text{PbI}_4$ (NoA, blue line), and $(4\text{Cl-C}_6\text{H}_4\text{NH}_3)_2\text{PbI}_4$ (4Cl-PhA, red line).

Methods

Improper flexoelastic model. It has been shown earlier that ordered LHPs structures can be treated as composite L1/L2 systems with coherent interfaces, although the definition of the L1 and L2 bulk materials must be chosen with care.¹ Such a framework allows relevant analysis of electronic and dielectric properties of the composite.^{1,2} To investigate mechanical properties, a first simple approach may be inspired by the elastic model used to predict the influence of lattice mismatch during epitaxial growth of conventional semiconductor heterostructures having a coherent interface.^{3,4} For an epitaxial layer with a low lattice mismatch ($\epsilon_{11}=\epsilon_{22}$) on a rigid (001) zinc-blende substrate, the out of plane strain reads $\epsilon_{33}=(-2C_{12}\epsilon_{11})/C_{11}$. It can be derived using the relation between stress and strain tensors:

$$\begin{pmatrix} \sigma_{11} \\ \sigma_{22} \\ \sigma_{33} \end{pmatrix} = \begin{pmatrix} C_{11} & C_{12} & C_{12} \\ C_{12} & C_{11} & C_{12} \\ C_{12} & C_{12} & C_{11} \end{pmatrix} \begin{pmatrix} \epsilon_{11} \\ \epsilon_{22} \\ \epsilon_{33} \end{pmatrix} \quad (1)$$

and the condition for a free (001) surface ($\sigma_{33}=0$). Alternatively, the same result can be obtained by minimizing the elastic free energy:

$$F = \frac{1}{2}V [C_{11}(\epsilon_{11}^2 + \epsilon_{22}^2 + \epsilon_{33}^2) + 2C_{12}(\epsilon_{11}\epsilon_{22} + \epsilon_{11}\epsilon_{33} + \epsilon_{22}\epsilon_{33})], \quad (2)$$

with respect to ϵ_{33} (V is the volume of the layer).

This model must be adapted for LHPs. As an example, $(\text{BA})_2\text{MA}_{(n-1)}\text{Pb}_n\text{I}_{(3n+1)}$ can be approximated to an L1/L2 heterostructure with L1= $(n-1)\text{MAPbI}_3$ and L2= $(\text{BA})_2\text{PbI}_4$. Here, the elastic properties of both layers must be taken into account. Considering the transverse elastic approximation for L1= $(n-1)\text{MAPbI}_3$:

$$\begin{pmatrix} \sigma_{11,L1} \\ \sigma_{22,L1} \\ \sigma_{33,L1} \end{pmatrix} = \begin{pmatrix} C_{11,L1} & C_{12,L1} & C_{13,L1} \\ C_{12,L1} & C_{11,L1} & C_{13,L1} \\ C_{13,L1} & C_{13,L1} & C_{33,L1} \end{pmatrix} \begin{pmatrix} \epsilon_{11,L1} \\ \epsilon_{22,L1} \\ \epsilon_{33,L1} \end{pmatrix}. \quad (3)$$

Then, the total elastic energy of the L1/L2 composite heterostructure is given by:

$$\begin{aligned} F &= \frac{1}{2}Sl_{L1} [C_{11,L1}(\epsilon_{11,L1}^2 + \epsilon_{22,L1}^2 + \epsilon_{33,L1}^2) + 2C_{12,L1}(\epsilon_{11,L1}\epsilon_{22,L1} + \epsilon_{11,L1}\epsilon_{33,L1} + \epsilon_{22,L1}\epsilon_{33,L1})] \\ &+ \frac{1}{2}Sl_{L2} [C_{11,L2}(\epsilon_{11,L2}^2 + \epsilon_{22,L2}^2) + C_{33,L2}\epsilon_{33,L2}^2 + 2C_{12,L2}\epsilon_{11,L2}\epsilon_{22,L2} + 2C_{13,L2}(\epsilon_{11,L2}\epsilon_{33,L2} + \epsilon_{22,L2}\epsilon_{33,L2})] \end{aligned} \quad (4)$$

where S is the surface of the coherent interface, $l_{L1}=(n-1)c_{3D}$ and $l_{L2}=c_{2D}$ are the thicknesses of the two layers, c_{2D} and c_{3D} are the stacking parameters of $(\text{BA})_2\text{PbI}_4$ and MAPbI_3 , respectively. The two layers share the same

in-plane lattice parameter a leading to the following strain components:

$$\begin{aligned}\epsilon_{11,L1} &= \epsilon_{22,L1} = (a - a_{3D})/a_{3D} \\ \text{and } \epsilon_{11,L2} &= \epsilon_{22,L2} = (a - a_{2D})/a_{2D}.\end{aligned}$$

The conditions for free strain relaxation along the stacking axis lead to:

$$\begin{aligned}\epsilon_{33,L1} &= (-2C_{12,L1}\epsilon_{11,L1})/C_{11,L1} \\ \text{and } \epsilon_{33,L2} &= (-2C_{13,L2}\epsilon_{11,L2})/C_{11,L2}.\end{aligned}$$

Finally, the equilibrium in-plane lattice parameter a_{eq} is derived by minimizing the total energy, yielding:

$$a_{eq} = \frac{\frac{K_{L1}}{a_{3D}} + \frac{K_{L2}}{a_{2D}}}{\frac{K_{L1}}{a_{3D}^2} + \frac{K_{L2}}{a_{2D}^2}} \quad (5)$$

$$\text{with } K_{L1} = (n-1)c_{3D} \left(C_{11,L1} + C_{12,L1} - 2\frac{C_{12,L1}^2}{C_{11,L1}} \right) \text{ and } K_{L2} = c_{2D} \left(C_{11,L2} + C_{12,L2} - 2\frac{C_{13,L2}^2}{C_{33,L2}} \right).$$

Noteworthy, this result allows recovering the two limiting cases: for $n=1$ ($K_{L1}=0$), $a_{eq}=a_{2D}$ and for $n=\infty$ ($K_{L1} \gg K_{L2}$), $a_{eq}=a_{3D}$. Also, in the special case of a vanishing lattice mismatch ($a_{2D}=a_{3D}$), the trivial result $a_{eq}=a_{2D}=a_{3D}$ is recovered for all n -values.

Unfortunately, measurements of elastic constants in MAPbI₃ (L1) remain scarce and reported values come from indirect spectroscopies performed at higher temperatures with large error bars.^{5,6} In addition, to the best of our knowledge, no values have been reported for their 2D counterpart (L2). However, we can infer relationships from the nature of both materials as well as from previous experimental results. The tetragonal phase of MAPbI₃ can be considered having the same elastic constants on all directions, *i.e.* $C_{33,L1} = C_{11,L1}$ and $C_{13,L1} = C_{12,L1}$. (BA)₂PbI₄ can be regarded as a $n=1$ slice of MAPbI₃. Thus, the in-plane elasticity of L2 is kept identical to the one of L1, *i.e.* $C_{11,L2} = C_{11,L1}$ and $C_{12,L2} = C_{12,L1}$. On the other hand, the out-of-plane elasticity, involving the large organic cations, is expected to be much weaker. Therefore, $C_{33,L2} = C_{33,L1}/2$ and $C_{13,L2} = C_{13,L1}/2$ seems a reasonable choice. As a first guess, we choose $C_{11,L1} = 20$ GPa and $C_{12,L1} = 15$ Gpa.

Meanwhile, we stress that the qualitative trend does not much depend on the precise values of the elastic constants: the model predicts a progressive increase of the in-plane parameter as a function of n , which is underestimated as compared to experimental structural parameters (Fig. S1). The deficiency of such a pure elastic model can be traced back to additional rotational degrees of freedom, namely octahedral tilting, which also afford a path to relax the accumulated mechanical energy. Indeed, it is well known that layered and 3D perovskites undergo both in-plane β_{010} and out-of-plane δ_{010} octahedral tilts (Fig. S2), which have been shown

to affect their electronic properties.⁷ It is also known that owing to symmetry properties (halide perovskites are improper ferroelastic materials) the coupling between these rotations and strain components is linear-quadratic.⁸ Experimental data (Table S1), show that δ_{010} of L2 is the most affected for increasing n-values.

Therefore, we modify our model considering that L1 reacts in a purely elastic manner, whereas L2 relaxes the strain through a variation of the δ_{010} angle, *i.e.* $C_{33,L2} = 0$. Then, the free energy of L2 reads:

$$F_{L2} = Sc_{2D} \left[C_{11,L2}(\epsilon_{11,L2}^2 + \epsilon_{22,L2}^2) + C_{12,L2}\epsilon_{11,L2}\epsilon_{22,L2} + \frac{1}{2}k_2\delta_{010}^2 + \frac{1}{4}k_4\delta_{010}^4 + \frac{1}{2}\lambda\delta_{010}^2\epsilon_{11,L2} \right]. \quad (6)$$

Again, we use $\epsilon_{11,L2} = \epsilon_{22,L2}$. This leads to an expression similar to (5) for a_{eq} :

$$a_{eq} = \frac{\frac{K_{L1}}{a_{3D}} - \frac{c_{2D}}{a_{2D}} \left(\frac{\lambda k_2}{k_4} + \frac{\lambda^2}{2k_4} \right)}{\frac{K_{L1}}{a_{3D}^2} - c_{2D} \frac{\lambda^2}{2k_4 a_{2D}^2}} \quad (7)$$

Once more, physical parameters are needed and available data is currently not sufficient to perform a full translation-rotation mechanical analysis at the same level as the one performed in some 3D perovskite oxides.⁹ Neglecting the term $\lambda k_2/k_4$ allows defining a single K_{L2} parameter from (7), in a similar way than in (5):

$$K_{L2} = c_{2D} \frac{-\lambda^2}{2k_4}.$$

When considering $\lambda^2/(2k_4) = 12$ GPa, the elastic model leads to an excellent agreement with experimental data (Fig. 1b). Again, the qualitative trend does not much depend on the precise values of λ and k parameters. For instance, for $\lambda^2/(2k_4)$ ranging from 9 GPa to 16 GPa, the overall conclusions remain valid (Fig. S3).

Crystal and slab structures. Calculations of bulk properties are performed in periodic systems using the X-ray resolved geometries for n=1 to 4.^{10,11} In these structures, the stacking axis is along the (010) direction. In the devices of interest, the growth direction is not along the stacking axis but along the (101) direction. Thus, before constructing slabs for investigating effect of surface relaxation, we apply an orthorhombic to tetragonal distortion and optimize atomic position of these modified bulk structures. Next, we built 5-octahedron thick slabs oriented in the (101) direction keeping only one out of the two inorganic layers sandwiched between the organic layers to ensure computationally manageable structures. The resulting slabs contain up to 874 atoms. Last, atomic positions of these (101) slabs are relaxed, while keeping the bottom 2 layers frozen in the bulk configuration. Properties of unrelaxed and relaxed slabs are referred to by *bulk-like* and *surface*, respectively. For detailed description of the slab construction see [Supplementary Text I](#).

Density functional theory calculations. DFT calculations are conducted with the SIESTA code.¹² The non-local van der Waals density functional of Dion *et al.* corrected by Cooper (C09) is used for geometry optimizations.^{13,14} SOC is taken into account through the on-site approximation as proposed by Fernández-Seivane

*et al.*¹⁵ To prevent conflicts between the on-site treatment and the non-locality of C09, single points calculations are conducted with the revPBE functional on which C09 is based. The dipole induced in slabs is treated with the dipole correction as implemented in SIESTA.¹⁶ Core electrons are described with Troullier-Martins pseudopotentials.¹⁷ The valence wavefunction is developed over a double- ζ polarized basis set of finite-range numerical pseudoatomic orbitals.¹⁸ An energy cutoff of 150 Ry for real-space mesh size is used. Noteworthy, DFT underestimates the bandgap closing upon surface relaxation in RPPs with $n > 2$. Turning to larger supercells, *e.g.* doubled, is likely to allow for additional distortions, which in turn shall further close the bandgap. Unfortunately, such size doubling is computationally too demanding. Besides, for effective masses and complex spinor Bloch functions (Kane model) we used the ABINIT package¹⁹ with GGA-revPBE gradient correction for exchange-correlation,²⁰ ABINIT projector augmented-wave (PAW) datasets²¹ as pseudopotentials for Pb, I, and Cs and an energy cutoff of 19 Ha (517 eV) for the plane-wave basis set. Primitive cells were used for the computation of the electronic band dispersions with Monkhorst-Pack grids for reciprocal space integration of: $4 \times 4 \times 1$ for $n=1$ and $2 \times 2 \times 4$ for $n=2, 3$ and 4 . Spin-orbit coupling was included in all calculations. As plane wave calculations are more demanding than the localized basis sets counterpart, organic cations have been substituted by Cs atoms. This substitution is known to leave the band dispersion unaffected close to the Fermi level and, in fact, for $n=3$ we obtain a comparable bandgap closing (128 meV) and similar spinorial components than with SIESTA and all atoms.

Localized density of states. LDOS is a function of energy and position describing the space-resolved density of states (DOS):

$$LDOS(\vec{r}, \epsilon) = \sum_i \langle \Psi_i | \vec{r} \rangle \langle \vec{r} | \Psi_i \rangle \delta(\epsilon - \epsilon_i).$$

Plots are obtained by the integration over a window of energy $\Delta\epsilon$ of 10 meV around the CBM and VBM (Fig. 3c and Fig. S7a,b). Profiles $\rho(z)$ (Fig. S7c), where z is along the (101) direction, are then obtained through:

$$\rho_{\text{CBM}}(z) = \int_{x,y} \int_{\epsilon_{\text{CBM}}}^{\epsilon_{\text{CBM}} + \Delta\epsilon} LDOS(x, y, z, \epsilon) dx dy d\epsilon,$$

and

$$\rho_{\text{VBM}}(z) = \int_{x,y} \int_{\epsilon_{\text{VBM}} - \Delta\epsilon}^{\epsilon_{\text{VBM}}} LDOS(x, y, z, \epsilon) dx dy d\epsilon.$$

From those, we can compute the position barycenters (Fig. S7d) as:

$$z_{\text{CBM}} = \int_z \frac{z \rho_{\text{CBM}}(z)}{\rho_{\text{tot}}} dz, \text{ and } z_{\text{VBM}} = \int_z \frac{z \rho_{\text{VBM}}(z)}{\rho_{\text{tot}}} dz, \text{ with } \rho_{\text{tot}} = \int_z \rho(z) dz.$$

Kane model. Optical activity was investigated using Kane's model, used for classical semiconductors, and

compute Kane energies according to:^{22,23}

$$E_{P_{i,j,k}} = \frac{2}{m_e} |\langle \Psi_{VB,i} | -i\hbar \frac{\partial}{\partial x_k} | \Psi_{CB,j} \rangle|^2,$$

where the term in brackets corresponds to the dipolar matrix element between the i^{th} valence band and the j^{th} conduction band, and x_k to a crystal axis. This requires knowledge about the complex spinorial components of each band. Unfortunately, such data are not accessible in the SIESTA package¹² when spin-orbit coupling (SOC) is taken into account and we performed single point calculations with the ABINIT software.¹⁹

References

- [1] Even, J., Pedesseau, L. & Katan, C. Understanding quantum confinement of charge carriers in layered 2d hybrid perovskites. *ChemPhysChem* **15**, 3733 (2014).
- [2] Saponi, D., Kepenekian, M., Pedesseau, L., Katan, C. & Even, J. Quantum confinement and dielectric profiles of colloidal nanoplatelets of halide inorganic and hybrid organic-inorganic perovskites. *Nanoscale* **8**, 6369 (2016).
- [3] Bimberg, D., Grundmann, M. & Ledentsov, N. N. *Quantum Dot Heterostructures* (John-Wiley and Sons, 1999).
- [4] Vurgaftman, I. & Meyer, J. R. Band parameters for III-V compound semiconductors and their alloys. *J. Appl. Phys.* **89**, 5815 (2001).
- [5] Beecher, A. N. *et al.* Direct observation of dynamic symmetry breaking above room temperature in methylammonium lead iodide perovskite. *ACS Energy Lett.* **1**, 880–887 (2016).
- [6] Mante, P.-A., Stoumpos, C. C., Kanatzidis, M. G. & Yartsev, A. Electron-acoustic phonon coupling in single crystal $\text{CH}_3\text{NH}_3\text{PbI}_3$ perovskites revealed by coherent acoustic phonons. *Nat. Commun.* **8**, 14398 (2017).
- [7] Pedesseau, L. *et al.* Advances and promises of layered halide hybrid perovskite semiconductors. *ACS Nano* **10**, 9776–9786 (2016).
- [8] Even, J. Pedestrian guide to symmetry properties of the reference cubic structure of 3d all-inorganic and hybrid perovskites. *J. Phys. Chem. Lett.* **6**, 2238 (2015).
- [9] Knight, K. S. Parametrization of the crystal structures of centrosymmetric zone-boundary-tilted perovskites: an analysis in terms of symmetry-adapted basis-vectors of the cubic aristotype phase. *Can. Mineral.* **47**, 381–400 (2009).
- [10] Billing, D. G. & Lemmerer, A. Synthesis, characterization and phase transitions in the inorganic-organic layered perovskite-type hybrids $[(\text{C}_n\text{H}_{2n+1}\text{NH}_3)_2\text{PbI}_4]$, $n=4, 5$ and 6 . *Acta Crystallogr. B* **63**, 735–747 (2007).
- [11] Stoumpos, C. C. *et al.* Ruddlesden-popper hybrid lead iodide perovskite 2d homologous semiconductors. *Chem. Mater.* **28**, 2852–2867 (2016).
- [12] Soler, J. M. *et al.* The siesta method for ab initio order-n materials simulation. *J. Phys.: Condens. Matter* **14**, 2745–2779 (2002).
- [13] Dion, M., Rydberg, H., Schröder, E., Langreth, D. C. & Lundqvist, B. I. Van der waals density functional for general geometries. *Phys. Rev. Lett.* **92**, 246401 (2004).
- [14] Cooper, V. R. Van der waals density functional: An appropriate exchange functional. *Phys. Rev. B* **81**, 161104(R) (2010).
- [15] Fernández-Seivane, L., Oliveira, M. A., Sanvito, S. & Ferrer, J. On-site approximation for spin-orbit coupling in linear combination of atomic orbitals density functional methods. *J. Phys.: Condens. Matter* **18**, 7999 (2006).
- [16] Bengtsson, L. Dipole correction for surface supercell calculations. *Phys. Rev. B* **59**, 12301 (1999).
- [17] Troullier, N. & Martins, J. L. Efficient pseudopotentials for plane-wave calculations. *Phys. Rev. B* **43**, 1993–2006 (1991).
- [18] Artacho, E., Sánchez-Portal, D., Ordejón, P., García, A. & Soler, J. M. Linear-scaling *ab-initio* calculations for large and complex systems. *Phys. Status Solidi B* **215**, 809–817 (1999).
- [19] Gonze, X. *et al.* Abinit: First-principles approach to material and nanosystem properties. *Comput. Phys. Commun.* **180**, 2582–2615 (2009).
- [20] Zhang, Y. & Yang, W. Comment on “generalized gradient approximation made simple”. *Phys. Rev. Lett.* **80**, 890 (1998).
- [21] Torrent, M., Jollet, F., Bottin, F., Zérah, G. & Gonze, X. Implementation of the projector augmented-wave method in the abinit code: Application to the study of iron under pressure. *Comput. Mater. Sci.* **42**, 337–351 (2008).
- [22] Kane, E. O. *Semiconductors and Semimetals* (Academic Press, 1966).
- [23] Chuang, S.-L. & Chang, S. k-p method for strained wurtzite semiconductors. *Phys. Rev. B* **54**, 2491–2504 (1996).

The role of lattice mismatch on the emergence of surface states in 2D hybrid perovskite quantum wells

Supplementary information

M. Kepenekian,^{1,*} B. Traore,¹ J.-C. Blancon,² L. Pedesseau,³ H. Tsai,^{2,4} W. Nie,² C. C. Stoumpos,⁵
M. G. Kanatzidis,⁵ J. Even,³ A. D. Mohite,² S. Tretiak,^{2,†} and C. Katan^{1,‡}

¹Univ Rennes, ENSCR, INSA Rennes, CNRS, ISCR – UMR 6226, F-35000 Rennes, France

²Los Alamos National Laboratory, Los Alamos, NM 87545, USA

³Univ Rennes, INSA Rennes, CNRS, FOTON – UMR 6082, F-35000 Rennes, France

⁴Department of Materials Science and Nanoengineering, Rice University, Houston, TX 77005, USA

⁵Department of Chemistry, Northwestern University, Evanston, IL 60208, USA

Elastic model for layered hybrid perovskites

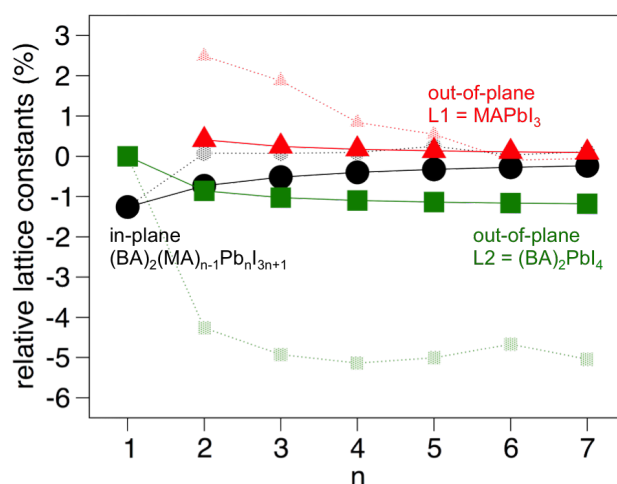


Figure S1 | Purely elastic model for LHPs. In-plane expansion and out-of-plane contractions of lattice constants for $(\text{BA})_2(\text{MA})_{n-1}\text{Pb}_n\text{I}_{3n+1}$ and the L1 and L2 layers from a purely elastic model. The room-temperature structures of MAPbI_3 and $(\text{BA})_2\text{PbI}_4$ serve as references for L1 and L2 structures, respectively. Shaded symbols correspond to experimental data.

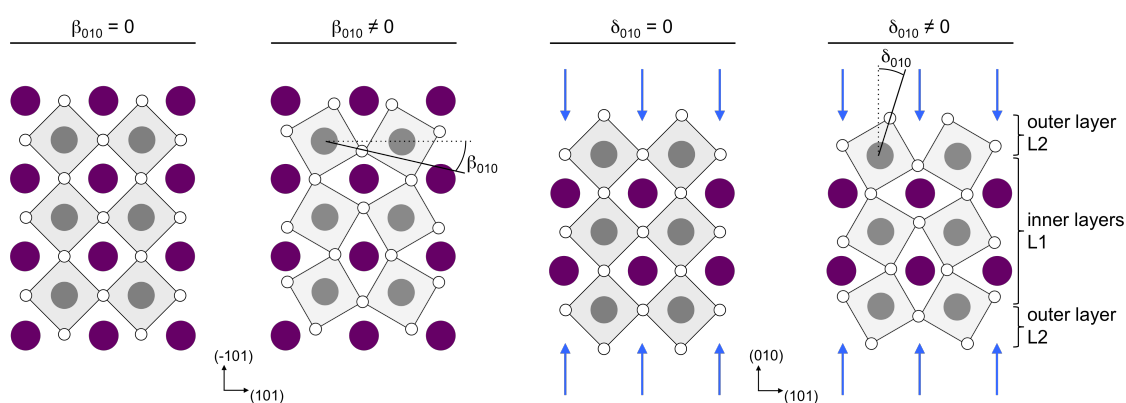


Figure S2 | Schematic of β_{010} and δ_{010} angles in layered hybrid perovskites for $n=3$.

Table S1 | Layer average β_{010} and δ_{010} angles. Values are taken from experimental data for the X-ray resolved structures of MAPbI₃ ($n=\infty$),¹ (BA)₂PbI₄ ($n=1$),² and the inner and outer layers of (BA)₂(MA) _{$n-1$} Pb _{n} I_{3 $n+1$} .³

	layer	β_{010} (°)	δ_{010} (°)		layer	β_{010} (°)	δ_{010} (°)
	$n=\infty$	0.85	6.20	$n=5$	outer	0.00	9.95
	$n=1$	12.27	5.78		inner	0.00	6.76
	$n=2$	outer	0.00	$n=6$	outer	0.00	10.10
		inner	0.00		inner	0.00	5.81
	$n=3$	outer	0.00	$n=7$	outer	0.00	10.18
		inner	0.00		inner	0.00	7.66
	$n=4$	outer	0.00				
		inner	0.00				

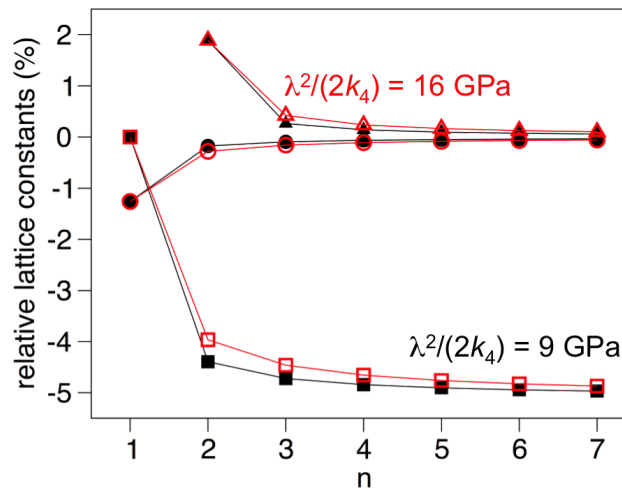


Figure S3 | Improper flexoelastic model for LHPs. In-plane expansion and out-of-plane contractions of lattice constants for (BA)₂(MA) _{$n-1$} Pb _{n} I_{3 $n+1$} and the L1 and L2 layers from the flexoelastic model using $\lambda^2/(2k_4)=9$ GPa (black symbols) and 16 GPa (red symbols).

(BA)₂(MA) _{$n-1$} Pb _{n} I_{3 $n+1$} RPP ($n=1$ to 4) from bulk to surface

Text I | (101) surface construction

Starting from the X-ray structures of (BA)₂(MA) _{$n-1$} Pb _{n} I_{3 $n+1$} (BA = butylammonium, MA = methylammonium) with $n=1$ to 4,^{3,4} we apply an orthorhombic to tetragonal distortion, *i.e.* the norms of in-plane cell vectors a and c are averaged to $a' = (a + c)/2$. It leads to a contraction (resp. dilatation) of a (resp. c). For $n=2$ to 4, the distortion is less than 0.5%. It is about 1% for $n=1$ (Table S2).

DFT relaxation of atomic positions is then performed for these modified bulk structures. Next, starting from the relaxed atomic positions we built slabs oriented in the (101) direction. Because of the orthorhombic to tetragonal transformation, the latter step is straightforward. To reach a computationally manageable structure, we further reduce the number of atoms by keeping one of the two inorganic layers sandwiched between organic layers (Fig. S4). The resulting 5-octahedron thick slabs contain 460, 598, 736 and 874 atoms per cell for $n=1, 2, 3$ and 4, respectively. Properties of these slabs are denoted as *bulk-like* properties. Worth noticing, all slabs present a global defect of 2 electrons. Along self-consistent calculations, it is compensated by a background charge density.

Then, to describe the surface, atomic positions of these (101) slabs are relaxed, while keeping the bottom 2 layers frozen in the bulk configuration. Properties of these slabs are denoted as *surface* properties. Noteworthy, considering also 4-octahedron thick slabs, we verified that the limited thickness does not alter our conclusions.

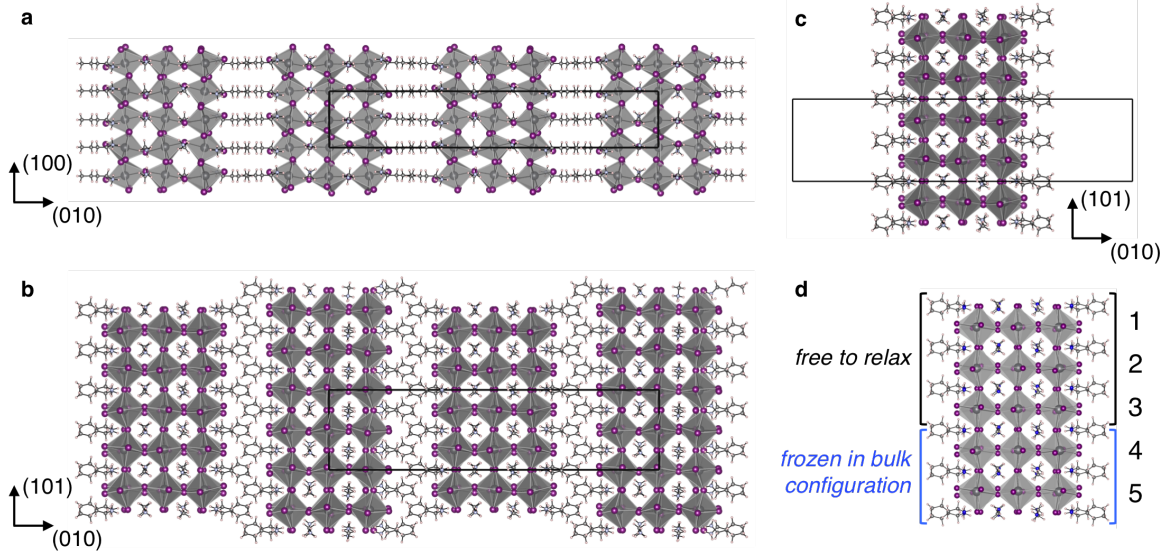


Figure S4 | From bulk to (101) surface. **a**, Modified structure of $n=3$ RPP where the original $Cmca$ orthorhombic cell is transformed to a tetragonal cell. The black line marks the unit cell of the modified bulk structures used in the calculation. **b**, Same structure reoriented along (101). The cell enlargement is limited by the tetragonal transformation. **c**, Only one inorganic layer is preserved, surrounded by 2 layers of the organic BA cations. **d**, A 5-octahedron thick slab is constructed. It is referenced as 'bulk-like' prior to relaxation. The bottom 2 layers of the slab are kept in bulk configuration, while the top 3 are allowed to relax freely, leading to the (101) surface. In all cases, Pb, I, N, C and H atoms are depicted in black, purple, blue, grey and pale pink, respectively.

Table S2 | Experimental (a , c) and modified ($a'=(a+c)/2$) norms of in-plane cell vectors for $(BA)_2(MA)_{n-1}Pb_nI_{3n+1}$ with $n=1$ to 4. η gives the relative error caused by the distortion, *i.e.* a contraction of \mathbf{a} and a dilatation of \mathbf{c} .

n	a' (Å)	a (Å)	η (%)	c (Å)	η (%)
1	8.784(4)	8.876(4)	-1.04	8.692(5)	1.06
2	8.903(0)	8.947(0)	-0.49	8.858(9)	0.50
3	8.902(6)	8.927(5)	-0.28	8.877(7)	0.28
4	8.904(5)	8.927(4)	-0.26	8.881(6)	0.26

DFT and semi-empirical simulation of bulk $(BA)_2(MA)_{n-1}Pb_nI_{3n+1}$ RPP ($n=1$ to 4)

Text II | Quantum and dielectric confinements and spatial overlap of wavefunctions

As in strongly confined quantum wells, bulk $(BA)_2(MA)_{n-1}Pb_nI_{3n+1}$ RPPs photophysical properties are dominated by mobile electron-hole (e-h) pairs strongly bound by a Coulombic interaction (*i.e.*, Wannier-like excitons). Room-temperature spectroscopy gives access to the resulting exciton binding energy E_b .⁵ It decreases from 380 meV and 270 meV for $n=1$ and 2, to 220 meV for $n=3$ and 4. Noteworthy, even for $n=4$, E_b remains substantial,

preventing room-temperature efficient electron-hole-pair ionisation in absence of multiple interfaces or internal field in the device.

The strength of E_b encompasses several physical phenomena that can be introduced gradually in a semi-empirical Bethe-Salpeter model.⁶⁻⁸ In addition to quantum confinement, evidenced by flat bands along the stacking directions, bulk RPPs exhibit dielectric confinement stemming from the contrast of high-frequency dielectric constant $\epsilon_\infty(z)$ between the organic and perovskite layers.⁸ The effect, strongest for $n=1$, decreases with increasing n . For $n=4$, $\epsilon_\infty(z)$ at the centre of the slab reaches almost the 3D MAPbI₃ value.⁸ Taking into account quantum and dielectric confinements leads to a large overestimation of E_b .⁸ However, the inclusion of wavefunctions (spatial expansion) in the evaluation of the exciton binding energy leads to excellent agreement between computed and experimental results. This evidences the dramatic effect of e-h overlap on the stability of the bound exciton states, which is used to further discuss exciton dissociation in the present work. Besides, ingredients of the model are obtained in the framework of DFT at a comparable level of theory than the one implemented here, thus supporting the validity of our approach.

DFT investigation of $(\text{BA})_2(\text{MA})_{n-1}\text{Pb}_n\text{I}_{3n+1}$ surfaces

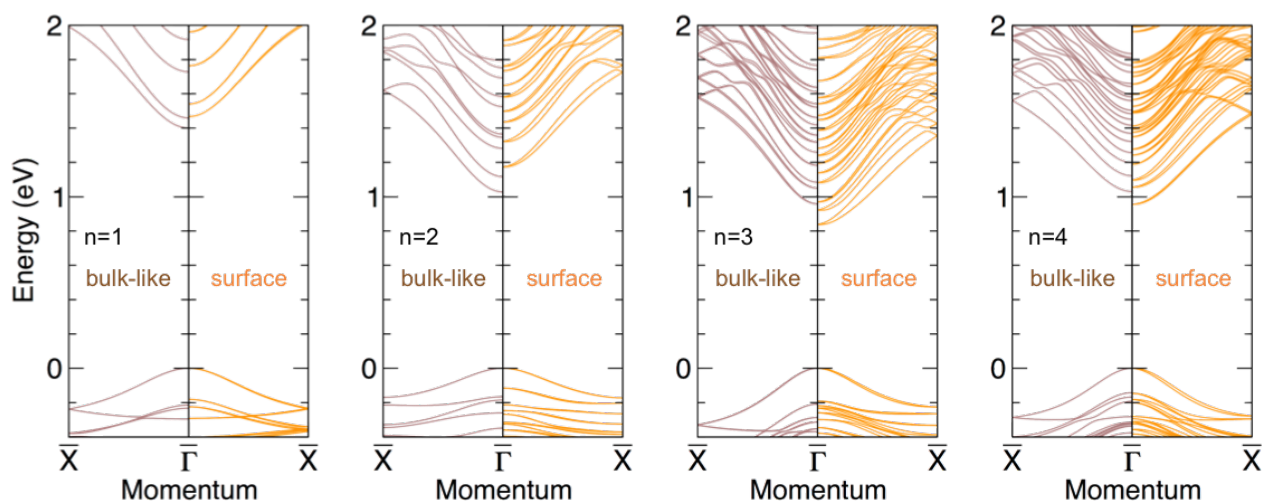


Figure S5 | (101) surface band structures. For each n value, the left panel shows the band structure of the bulk-like structure and the right panel the relaxed (101) surface band structure.

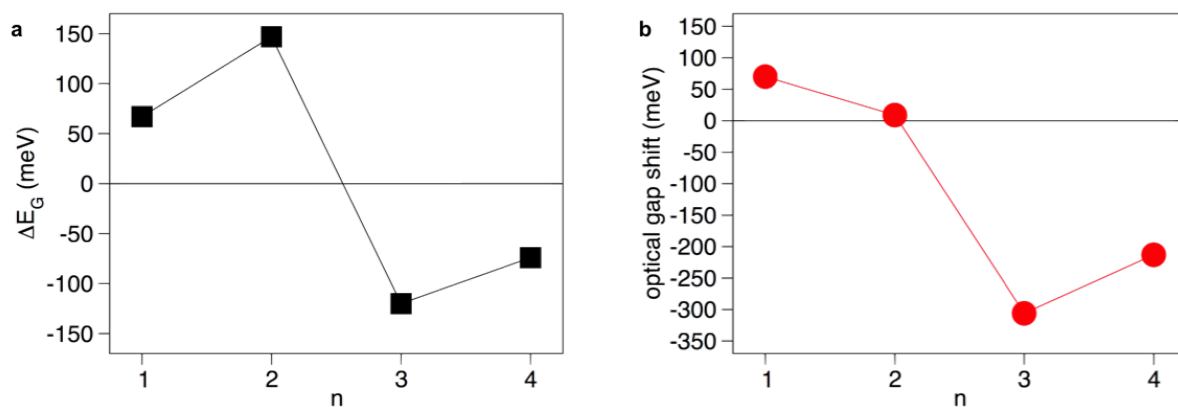


Figure S6 | Gap shift. **a** DFT variation of E_G going from bulk-like to relaxed (101) surface. **b** Corresponding experimental shifts of the optical bandgap from exfoliated crystal to thin-film.⁵

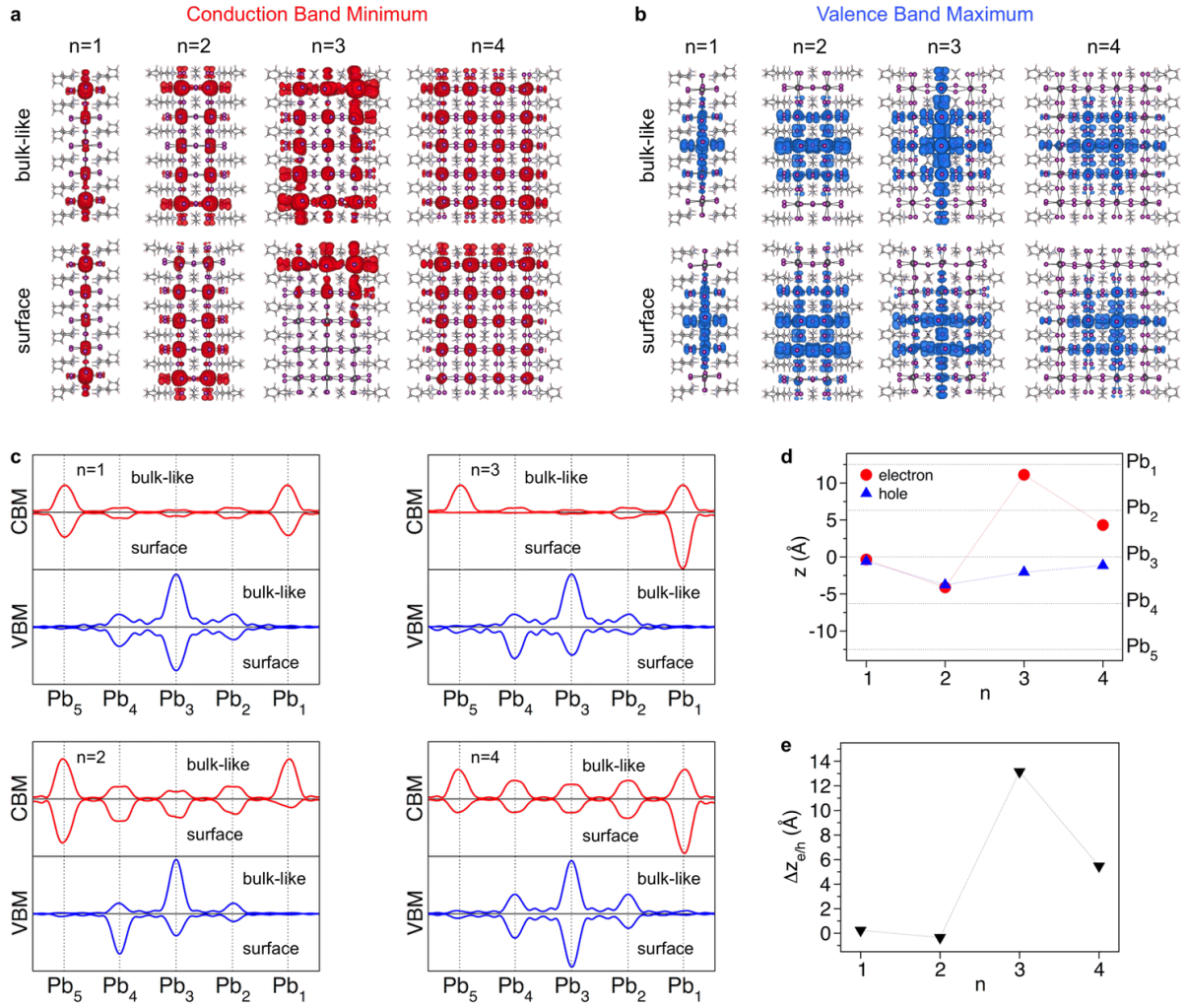


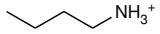
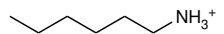
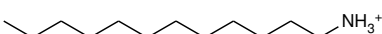
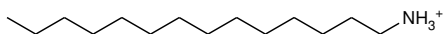
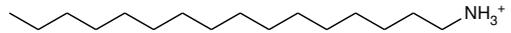
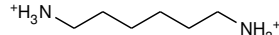
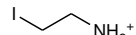
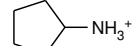
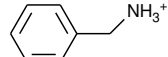
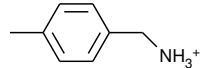
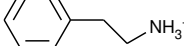
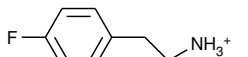
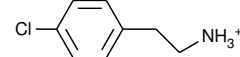
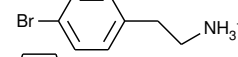
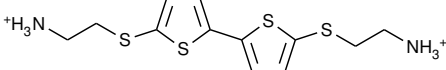
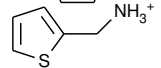
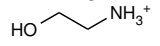
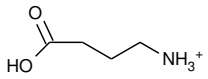
Figure S7 | Electron and hole localization in (101) RPP surfaces. **a**, LDOS at the conduction band minimum (CBM) in bulk-like and (101) surface slabs for $n=1$ to 4 RPPs. **b**, Same for the valence band maximum (VBM). **c**, LDOS profiles along the (101) direction for CBM and VBM of $n=1$ to 4 surfaces. The positions are indicated with respect to the five planes formed by lead atoms in the slab. Pb_5 points to the bottom plane that remains in bulk configuration, whereas Pb_1 is the top layer, *i.e.* the (101) surface. For $n \geq 3$, the CBM gets localized at the surface with depletion in deeper regions. In all structures, the VBM tends to move away from the surface. **d**, Position of the barycentres z_e and z_h of electron (CBM) and hole (VBM) states for the (101) slab. For all n , in bulk-like structures, the barycentres of CBM and VBM are always localized at the center of the slab. **e**, Electron-hole separation $\Delta z_{e/h} = z_e - z_h$ (in Å) for $n=1$ to 4 surfaces. For $n \leq 2$, electron and holes overlap, whereas for $n \geq 3$ a clear segregation occurs with a maximum separation for $n=3$ with $\Delta z_{e/h} > 10$ Å.

Table S3 | Kane energies (eV) computed for the $n=3$ RPP for bulk-like and (101) surface slabs. As the conduction bands (CB) and valence bands (VB) of interest are doubly degenerated, we use the notation $CBM_{1,2}$, $VBM_{1,2}$, $CBM_{3,4}$ and $VBM_{3,4}$.

	Bulk-like							
	$VBM_{1,2}$				$VBM_{3,4}$			
	x	y	z	norm	x	y	z	norm
$CBM_{1,2}$	0.468	0.536	0.784	1.059	0.010	0.014	0.042	0.045
$CBM_{3,4}$	0.737	0.870	0.732	1.355	0.166	0.212	0.072	0.279
	Surface							
	$VBM_{1,2}$				$VBM_{3,4}$			
	x	y	z	norm	x	y	z	norm
$CBM_{1,2}$	0.164	0.186	0.460	0.523	0.018	0.024	0.008	0.031
$CBM_{3,4}$	0.086	0.116	0.134	0.197	0.010	0.006	0.010	0.015

Design of layered hybrid perovskites

Table S4 | Chemical nomenclature and references for Fig. 4a.

	Name	Formula	Ref.
BA	Butylammonium		2
PeA	Pentylammonium		4
HA	Hexylammonium		4
NoA	Nonylammonium		9
DoDA	Dodecylammonium		10
TeDA	Tetradecylammonium		10
HeDA	Hexadecylammonium		10
ODA	Octadecylammonium		10
HA ₂	1,6-diammoniohexane		11
IEA	2-iodoethylammonium		12
NCEA	2-cyanoethylammonium		13
cPeA	cyclopentylammonium		14
PhMA	phenylmethylammonium		15
4MPhMA	4-methylphenylmethylammonium		16
1-PhEA	1-phenylethylammonium		17
4F-PhEA	4-fluorophenylethylammonium		18
4Cl-PhA	4-chlorophenylammonium		19
4Br-PhA	4-bromophenylammonium		20
(ThEA) ₂	5-ammoniummethylsulfanyl-2,2'-bithiophene		21
ThMA	2-thienylmethylammonium		22
2-hydroxyEA	2-hydroxyethylammonium		23
HOBA	4-ammoniobutanoic		24

References

- [1] Dang, Y. *et al.* Bulk crystal growth of hybrid perovskite material $\text{CH}_3\text{NH}_3\text{PbI}_3$. *CrystEngComm* **17**, 665–670 (2015).
- [2] Mitzi, D. B. Synthesis, crystal structure, and optical and thermal properties of $(\text{C}_4\text{H}_9\text{NH}_3)_2\text{Ml}_4$ (M = Ge, Sn, Pb). *Chem. Mater.* **8**, 791 (1996).
- [3] Stoumpos, C. C. *et al.* Ruddlesden-popper hybrid lead iodide perovskite 2d homologous semiconductors. *Chem. Mater.* **28**, 2852–2867 (2016).
- [4] Billing, D. G. & Lemmerer, A. Synthesis, characterization and phase transitions in the inorganic-organic layered perovskite-type hybrids $[(\text{C}_n\text{H}_{2n+1}\text{NH}_3)_2\text{PbI}_4]$, $n=4, 5$ and 6 . *Acta Crystallogr. B* **63**, 735–747 (2007).
- [5] Blancon, J.-C. *et al.* Extremely efficient internal exciton dissociation through edge states in layered 2d perovskites. *Science* **355**, 1288–1292 (2017).
- [6] Pedesseau, L. *et al.* Advances and promises of layered halide hybrid perovskite semiconductors. *ACS Nano* **10**, 9776–9786 (2016).
- [7] Smith, M. D. *et al.* Decreasing the electronic confinement in layered perovskites through intercalation. *Chem. Sci.* **8**, 1960–1968 (2017).
- [8] Blancon, J.-C. *et al.* Strongly bound excitons in ruddlesden-popper 2d perovskites arXiv:1710.07653.
- [9] Lemmerer, A. & Billing, D. G. Synthesis, characterization and phase transitions of the inorganic-organic layered perovskite-type hybrids $[(\text{C}_n\text{H}_{2n+1}\text{NH}_3)_2\text{PbI}_4]$, $n=7, 8, 9$ and 10 . *Dalton Trans.* **41**, 1146–1157 (2012).
- [10] Billing, D. G. & Lemmerer, A. Synthesis, characterization and phase transitions of the inorganic-organic layered perovskite-type hybrids $[(\text{C}_n\text{H}_{2n+1}\text{NH}_3)_3\text{PbI}_4]$ ($n = 12, 14, 16$ and 18). *New J. Chem.* **32**, 1736–1746 (2008).
- [11] Mousdis, G. A., Papavassiliou, G. C., Raptopoulou, C. P. & Terzis, A. Preparation and characterization of $[\text{H}_3\text{N}(\text{CH}_2)_6\text{NH}_3]\text{PbI}_4$ and similar compounds with a layered perovskite structure. *J. Mater Chem.* **10**, 515–518 (2000).
- [12] Sourisseau, S. *et al.* Reduced band gap hybrid perovskites resulting from combined hydrogen and halogen bonding at the organic-inorganic interface. *Chem. Mater.* **19**, 600–607 (2007).
- [13] Mercier, N., Louvain, N. & Bia, W. Structural diversity and retro-crystal engineering analysis of iodometalate hybrids. *CrystEngComm* **11**, 720–734 (2009).
- [14] Billing, D. G. & Lemmerer, A. Inorganic-organic hybrid materials incorporating primary cyclic ammonium cations: The lead iodide series. *CrystEngComm* **9**, 236–244 (2007).
- [15] Papavassiliou, G. C., Mousdis, G. A., Raptopoulou, C. P. & Terzis, A. Preparation and characterization of $(\text{C}_6\text{H}_5\text{CH}_2\text{NH}_3)_2\text{PbI}_4$, $(\text{C}_6\text{H}_5\text{CH}_2\text{CH}_2\text{SC}(\text{NH}_2)_2)_3\text{PbI}_5$ and $(\text{C}_{10}\text{H}_7\text{CH}_2\text{NH}_3)\text{PbI}_3$ organic-inorganic hybrid compounds. *Z. Naturforsch., B* **54**, 1405–1409 (1999).
- [16] Papavassiliou, G. C., Mousdis, G. A., Raptopoulou, C. P. & Terzis, A. Some new luminescent compounds based on 4-methylbenzylamine and lead halides. *Z. Naturforsch., B* **55**, 536–540 (2000).
- [17] Billing, D. G. Bis(1-phenylethylammonium) tetraiodoplumbate(II). *Acta Cryst. E* **58**, m669–m671 (2002).
- [18] Kikuchi, K., Takeoka, Y., Rikukawa, M. & Sanui, K. Structure and optical properties of lead iodide based two-dimensional perovskite compounds containing fluorophenethylamines. *Curr. Appl. Phys.* **4**, 599–602 (2004).
- [19] Liu, Z. *et al.* Crystal structure of bis(4-chloroanilinium) tetraiodoplumbate(II), $(\text{ClC}_6\text{H}_4\text{NH}_3)_2\text{PbI}_4$. *Z. Kristallogr. NCS* **219**, 457–458 (2004).
- [20] Dai, H. *et al.* Crystal structure of bis(4-bromophenylaminium) tetraiodoplumbate(II), $(\text{BrC}_6\text{H}_4\text{NH}_3)_2\text{PbI}_4$. *Z. Kristallogr. NCS* **224**, 149–150 (2009).
- [21] Zhu, X.-H. *et al.* Effect of mono- versus di-ammonium cation of 2,2'-bithiophene derivatives on the structure of organic-inorganic hybrid materials based on iodo metallates. *Inorg. Chem.* **42**, 5330–5339 (2003).
- [22] Zhu, X.-H., Mercier, N., Riou, A., Blanchard, P. & Frère, P. $(\text{C}_4\text{H}_3\text{SCH}_2\text{NH}_3)_2(\text{CH}_3\text{NH}_3)\text{Pb}_2\text{I}_7$: non-centrosymmetrical crystal structure of a bilayer hybrid perovskites. *Chem. Commun.* 2160–2161 (2002).
- [23] Mercier, N., Poiroux, S., Riou, A. & Batail, P. Unique hydrogen bonding correlating with a reduced band gap and phase transition in the hybrid perovskites $(\text{HO}(\text{CH}_2)_2\text{NH}_3)_2\text{PbX}_4$ (X = I, Br). *Inorg. Chem.* **43**, 8361–8366 (2004).
- [24] Mercier, N. $(\text{HO}_2\text{C}(\text{CH}_2)_3\text{NH}_3)_2(\text{CH}_3\text{NH}_3)\text{Pb}_2\text{I}_7$: a predicted non-centrosymmetrical structure built up from carboxylic acid supramolecular synthons and bilayer perovskite sheets. *CrystEngComm* **7**, 429–432 (2005).